

High efficient bi-functional metasurface with linear polarization conversion and asymmetric transmission for terahertz region

Thi Quynh Hoa Nguyen* , Thi Minh Nguyen and Hong Quang Nguyen

School of Engineering and Technology, Vinh University, 182 Le Duan, Vinh 460000, Vietnam

E-mail: ntqhoa@vinhuni.edu.vn

Received 9 September 2024, revised 18 October 2024

Accepted for publication 29 October 2024

Published 11 December 2024



Abstract

Polarization control is crucial in contemporary photonics, but achieving broad bandwidths and high efficiencies remains a significant challenge. Here, we propose a wideband and high-efficiency metasurface designed for linear polarization conversion and asymmetric transmission (AT) in the terahertz region based on a three-layered chiral structure. By integrating a double-split ring resonator with a strip resonator, the proposed design can improve bandwidth and efficiency cross-polarization conversion and AT capabilities for a linearly polarized wave. The operating band for AT is 0.73–3.01 THz with an efficiency above 0.8, while the polarization conversion ratio exceeds 0.99 across the 0.56–3.94 THz range. The underlying physical mechanism behind wideband transmission polarization conversion is fully elucidated through theoretical analysis and the characterization of surface current distribution. The designed structure can be used in terahertz imaging, sensing, and communication.

Keywords: metasurface, polarization conversion, asymmetric transmission

1. Introduction

Terahertz (THz) technology, spanning frequencies from 0.1 to 10 THz, is a rapidly advancing field with significant potential for applications in imaging, non-destructive sensing, and communication systems [1, 2]. Nevertheless, conventional materials demonstrate limited electromagnetic (EM) response within the THz range, primarily due to the non-ionizing characteristics of THz radiation [3]. Recently, metasurfaces, the two-dimensional counterparts of metamaterials, have attracted growing interest for their ability to manipulate EM waves across a wide range of frequencies, from microwave and THz to visible light, enabling control over the amplitude [4–6], phase [7, 8], and polarization [9–11]. Since the asymmetric transmission (AT) effect was first demonstrated in 2006

[12], many designs of transmission polarization conversion with AT effect for linearly or circularly polarized waves have been developed for a wideband from microwave frequencies to optical frequencies [13–17]. AT refers to the phenomenon where EM waves can pass through a designed structure in one direction while being blocked in the opposite direction. This effect plays a crucial role in various fields, including imaging, sensing, and communication.

To achieve AT polarization conversion, various chiral metasurface structures, that can overcome the concept of directional transmission symmetry, have garnered significant attention in recent years. For instance, Zhao *et al* used chiral metasurface to achieve ultrabroadband for linear polarization conversion (LPC) and AT across a frequency range from 3.7 to 18 GHz; however, its AT efficiency was still low (~ 0.5) [18]. Similarly, Huang *et al* designed a three-layered chiral metasurface to achieve an ultra-wideband linear-polarization converter with excellent efficient AT characteristics at 4.6–14.0 GHz

* Author to whom any correspondence should be addressed.

and its AT parameter reached 0.7 at the same frequency region [19]. Furthermore, Zhang *et al* designed a three-layered chiral metasurface composed of cross-shaped structures, which showed an ultra-broadband PC from 0.41 to 2.38 THz for linearly polarized (LP) waves, but AT parameter was less than 0.64 [20]. The low efficiency of the AT effect can limit the practical application of chiral metamaterials. Therefore, developing chiral metasurfaces that exhibit the AT effect for LP waves across a broad bandwidth while maintaining high efficiency remains a significant challenge.

In this paper, we propose a wideband and high-efficiency bi-functional metasurface for LCP and AT in the THz region. The design is based on a three-layered chiral metasurface comprising orthogonal metal gratings, a metal resonator, and a polyimide dielectric spacer. By integrating a double-split ring resonator with a strip resonator, the proposed design enhances the bandwidth and efficiency of LCP and AT simultaneously. The metasurface demonstrates the ability to convert an incident LP wave to its orthogonal transmitted component, achieving a polarization conversion ratio (PCR) exceeding 0.99 across a broad frequency range of 0.56–3.94 THz. Additionally, it exhibits a high AT effect from 0.73 to 3.01 THz with an efficiency above 0.8. The working mechanism of the proposed metasurface is also thoroughly analyzed using theoretical analysis and surface current distribution analysis. These findings emphasize the considerable potential of the proposed structure for various THz applications such as imaging and communication.

2. Structure design and method

The schematic of the proposed bi-functional metasurface (BFM) with LCP and AT functionalities working at THz frequencies is illustrated in figure 1. The metasurface is composed of two orthogonal metal gratings, a metal resonator and two dielectric spacers. In this structure, the top and bottom orthogonal metallic gratings function as polarization selectors, while the middle metallic resonator, characterized by its diagonal symmetry, acts as a polarization converter. Specifically, the top metallic layer operates as a horizontal grating that selectively transmits y -polarization (TE) and reflects x -polarization (TM). On the other hand, the bottom metallic layer serves as a vertical grating that selects x -polarization and reflects y -polarization. The combination of the middle layer with the top and bottom gratings forms a Fabry–Pérot-like cavity [21]. To enhance the bandwidth and efficiency of the proposed structure, innovative geometric configurations for the polarization conversion resonator are being developed. In this design, we employ a combination of two resonators, a double-split ring associated with a strip (DSRCT), to create a polarization conversion metasurface with diagonal symmetry, aimed at designing an efficient wideband polarization conversion, as illustrated in figure 1(c). Moreover, the polarization selecting capability of the top and bottom

orthogonal metallic gratings enables the proposed structure to achieve a high-efficiency AT effect. Therefore, the proposed structure can simultaneously achieve high performance in both PCR and the AT effect. The metal layers are made of gold with conductivity of $4.56 \times 10^7 \text{ (S m)}^{-1}$. The thickness of the gold layers (t) is $0.3 \mu\text{m}$. Polyimide is used as the dielectric spacers with dielectric constant of 3.5 and a loss tangent of 0.0027.

To aid the optimize and analyze the proposed BFM structure, the commercial software CST Microwave Studio based a finite integration technique is conducted. In the simulation setup, the unit cell boundary conditions are applied in the x - and y - directions, while the z - direction has an open boundary condition. The design process of the proposed structure was systematically simulated to ensure optimized performance for polarization conversion and AT modes simultaneously. Initially, the dielectric thickness (d) and unit cell periodicity (P) were optimized to achieve the widest bandwidth and highest efficiency for the PCR and AT spectra across the target frequency range of 0.1 THz–10 THz. After optimizing these primary parameters, the remaining dimensions of the unit cells were carefully tuned to further enhance PCR and AT performance. The results of this design process are presented in the following section (Influence of Structural Parameters). Based on this design process, the optimized geometrical parameters of the unit cell for the proposed BFM are $P = 42 \mu\text{m}$, $d = 17 \mu\text{m}$, $R = 18.7 \mu\text{m}$, $b = 3 \mu\text{m}$, $c = 10 \mu\text{m}$, $i = 4 \mu\text{m}$, $l = 43.5 \mu\text{m}$, $w = 3 \mu\text{m}$, and $s = 6 \mu\text{m}$, as depicted in figures 1(b)–(d), respectively. It should be noted that the proposed metasurface has unit cell dimensions of $42 \mu\text{m} \times 42 \mu\text{m} \times 17 \mu\text{m}$, making it well-suited to standard fabrication techniques. The micro-scale structure is patterned using conventional photolithography, while polyimide and gold thin films are deposited via spin coating and sputtering, respectively [22, 23]. Transmission spectra of the metasurface in the THz range can be characterized using THz Time-Domain Spectroscopy (THz-TDS). The feasibility of fabricating our structure is demonstrated through several steps in the fabrication process. First, a layer of photoresist is spin-coated onto a substrate, such as a silicon wafer, and optical lithography is employed to pattern the bottom gratings. A 200-nm-thick gold layer is subsequently deposited via sputtering, and the photoresist is removed through a lift-off process to form the gold bottom gratings. Next, a 17- μm -thick polyimide layer is applied using spin coating. A second layer of photoresist is then spin-coated and patterned via optical lithography to define the resonator structure. Afterward, a 200-nm-thick gold layer is deposited by sputtering, and the photoresist is removed through lift-off to form the Au DSRCT-shaped resonator. Another 17- μm -thick polyimide layer is then applied using spin coating. In the final steps, a thin layer of photoresist is spin-coated and patterned using optical lithography to form the top gratings, followed by the deposition of a third 200-nm-thick gold layer via sputtering. The photoresist is again removed through lift-off, completing the fabrication of the gold top gratings and yielding the final device.

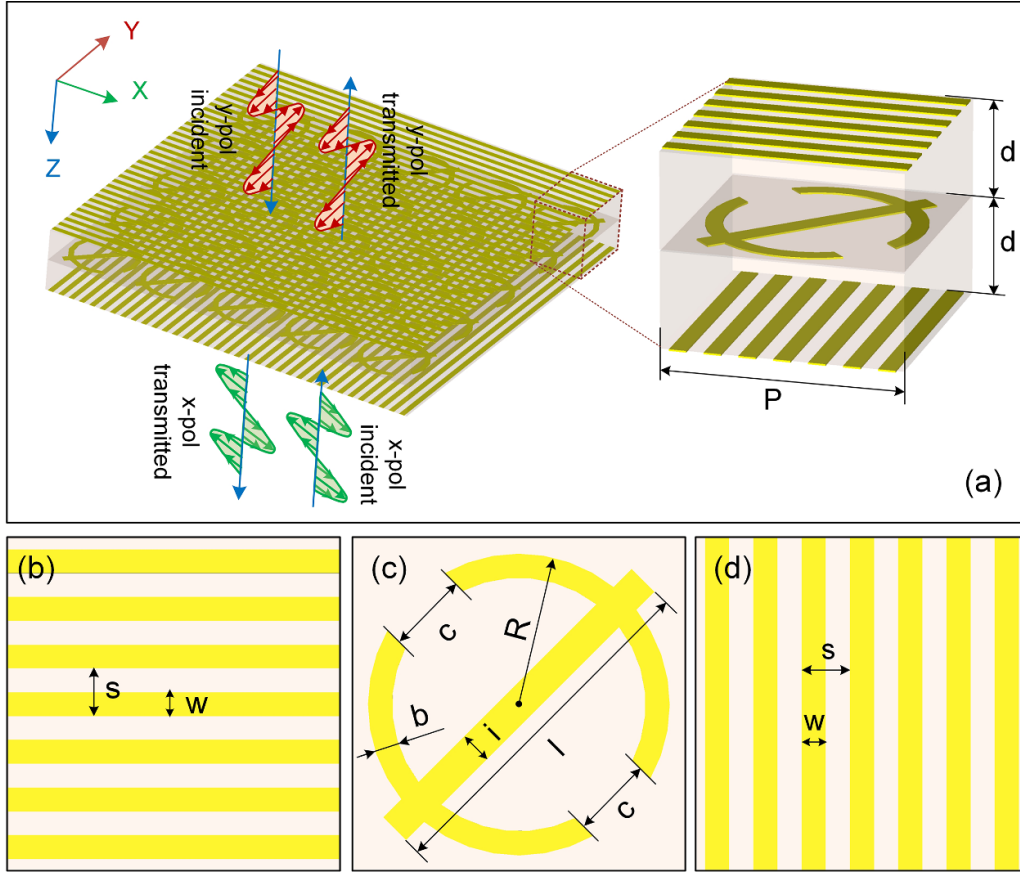


Figure 1. Schematic diagram for the proposed BFM structure for transmission cross-polarization conversion and asymmetric transmission: (a) 3D view and its enlarged unit cell and 2D view of (b) top metal gratings, (c) metal resonator, and (d) bottom metal gratings.

The Jones matrix (T) characterizes the relationship between the incident and transmitted waves, and is given by [24, 25]:

$$\begin{pmatrix} E_x^{tr} \\ E_y^{tr} \end{pmatrix} = \begin{bmatrix} t_{xx}^{f(b)} & t_{xy}^{f(b)} \\ t_{yx}^{f(b)} & t_{yy}^{f(b)} \end{bmatrix} \begin{pmatrix} E_x^{in} \\ E_y^{in} \end{pmatrix} = t_{lin}^{f(b)} \begin{pmatrix} E_x^{in} \\ E_y^{in} \end{pmatrix}. \quad (1)$$

Here, the superscripts f and b indicate the propagation of the EM waves in the forward ($+z$) and backward ($-z$) directions, respectively, while the subscripts x and y represent the polarization directions of the EM waves.

To assess the performance of LCP, a PCR is used. PCR is defined by equations (2) and (3) [26].

$$PCR_x = \frac{|t_{yx}|^2}{|t_{yx}|^2 + |t_{xx}|^2} \quad (2)$$

$$PCR_y = \frac{|t_{xy}|^2}{|t_{xy}|^2 + |t_{yy}|^2} \quad (3)$$

$$T_{ij} = |t_{ij}|. \quad (4)$$

Here, t_{ij} denotes the transmission coefficient of the transmitted wave polarized in the i direction caused by the j polarized incident wave ($i, j = x$ or y).

The AT parameter (Δ) for a LP wave is defined as the difference between the total transmission in the forward direction and the backward direction. This parameter measures the AT capability of the device and can be expressed as follows [26]:

$$\Delta_{lin}^x = |t_{xx}^f|^2 + |t_{yx}^f|^2 - |t_{yx}^b|^2 - |t_{xx}^b|^2 = |t_{yx}^f|^2 - |t_{xy}^f|^2 \quad (5)$$

$$\Delta_{lin}^y = -\Delta_{lin}^x. \quad (6)$$

3. Results and discussion

3.1. Performance characterizations

Figures 2(a) and (b) display the transmission coefficients (t_{xx} , t_{yx} , t_{xy} , t_{yy}) of the proposed BFM for the normally incident x -polarized and y -polarized waves propagating along the forward ($+z$) and backward ($-z$) directions, respectively. It is observed that the cross-polarization transmission coefficients (t_{xy} and t_{yx}) of the proposed BFM exceed 0.9 over a wide frequency range from 0.73 to 3.0 THz for normally incident forward y -polarized waves and backward x -polarized waves. Within this frequency band, five resonance frequencies can be observed at 0.72, 0.92, 1.37, 2.03 and 2.76 THz. Additionally, the co-polarization transmission coefficients (t_{yy} and t_{xx}) of the proposed BFM are below 0.015 over the aforementioned wide frequency range for both incident forward and backward

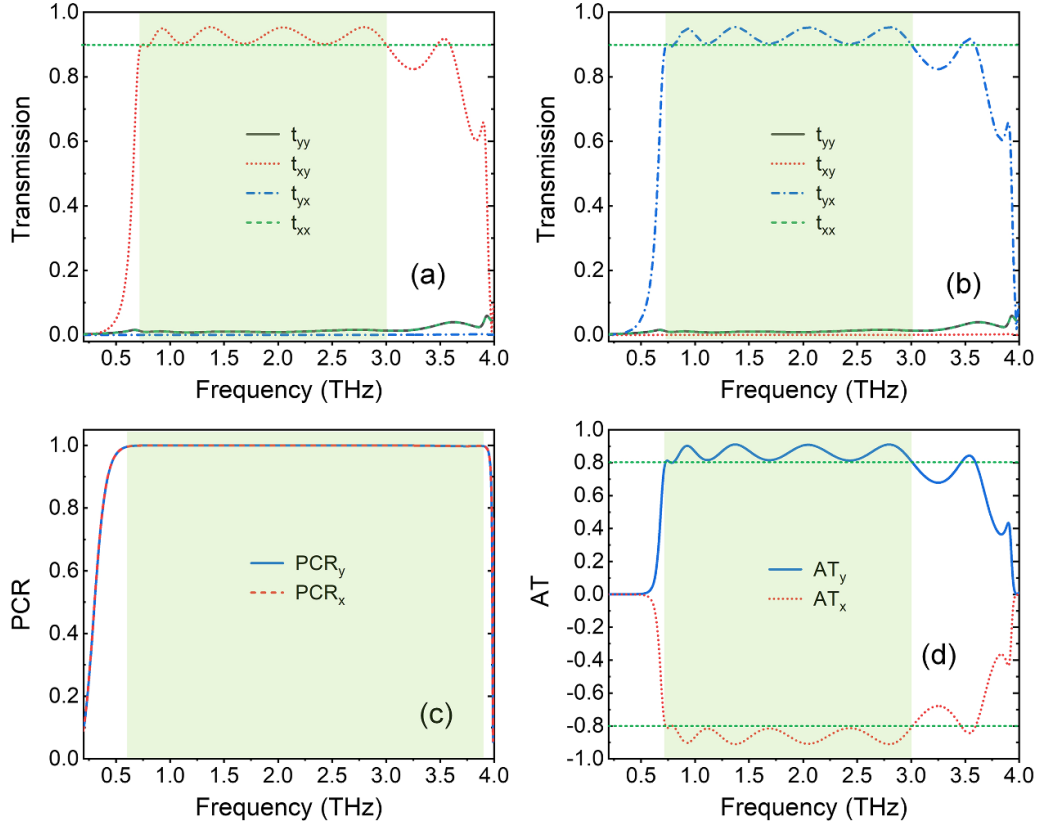


Figure 2. Amplitude of transmission efficiencies for (a) forward y -polarized wave and (b) backward x -polarized wave and (c) PCR and (d) AT spectra for forward y -polarized wave and backward x -polarized wave of the proposed metasurface.

x - and y - polarized waves. Meanwhile, the magnitudes of t_{yx} and t_{xy} are near zero across the entire frequency range for normal incident forward x - polarized waves and backward y - polarized waves, respectively. This reveals that the proposed BFM efficiently converts the linearly incident y -/ x - polarized waves along the $+z$ ($-z$) direction into transmitted x / y -polarized waves over wideband frequency range, respectively. And, there is no polarization conversion of the incident x -polarized wave along the $+z$ direction, or the y -polarized wave along the $-z$ direction. Figure 2(c) shows PCR_y and PCR_x for the incident forward y - polarized and backward x - polarized waves. The PCR remains above 0.99 in the wide frequency band of 0.56–3.94 THz under a normal incidence wave along forward y - polarized and backward x - polarized waves. The calculated relative bandwidth (RBW), defined as $RBW = 2(f_H - f_L)/(f_H + f_L)$ where f_H and f_L are the high and low limits of a frequency with efficiency above 0.99, respectively, reaches about 150.2%. Moreover, the AT efficiency is over 0.8 for forward y -polarized wave and backward x -polarized wave in the frequency range of 0.73–3.01 THz, with PBW of 124.9 %. (figure 2(d)). It indicates that the proposed BFM structure can achieve wideband LPC and AT characteristics.

To study the chirality property of the proposed BFM structure, we analyze the transmission coefficients for both left circularly polarized (LCP) and right circularly polarized

(RCP) light. The chirality parameter can be determined by examining the difference between the transmission of right-handed circularly polarized light (T_{RCP}) and left-handed circularly polarized light (T_{LCP}), known as circular dichroism (CD). The CD is calculated by equation [27]:

$$CD = T_{RCP} - T_{LCP} = (|t_{RR}|^2 + |t_{LR}|^2) - (|t_{RL}|^2 + |t_{LL}|^2) \quad (7)$$

where t_{RR} represents the transmission coefficient of RCP light caused by the incident RCP light, while t_{LR} denotes the transmission coefficient for LCP light caused by the incident RCP light. Similarly, t_{LL} refers to the transmission coefficient for LCP light caused by the incident LCP light, and t_{RL} indicates the transmission coefficient for RCP light caused by the incident LCP light. Figures 3(a) and (b) present the circular polarization transmission coefficients and CD spectrum for both forward and backward directions, respectively. The diagonal symmetry of the designed structure, which also exhibits mirror symmetry, results in a nearly equal response to LCP and RCP transmitted light, leading to a CD value close to zero, as illustrated in figures 3(a) and (b). This indicates that the designed BFM structure exhibits minimal chiral properties due to its symmetrical response to both LCP and RCP light.

To illustrate the contribution of the various resonators in the middle layer of the proposed metasurface to LCP and AT

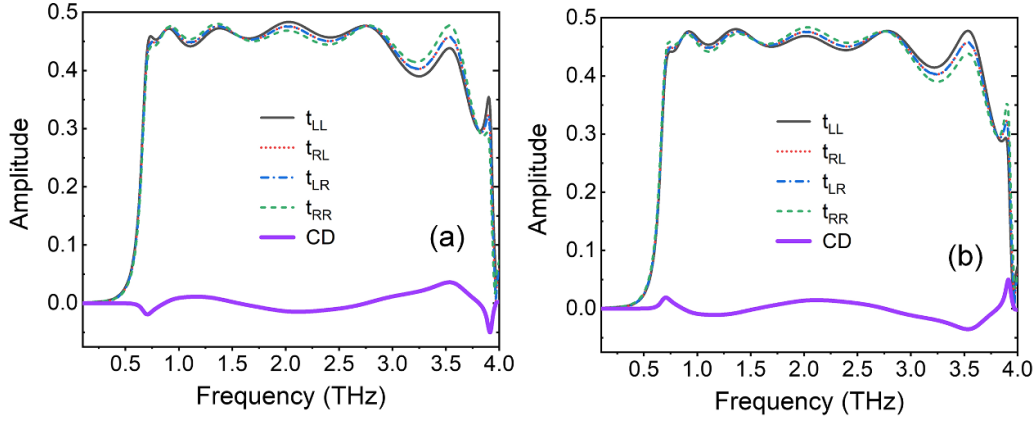


Figure 3. The circular polarization transmission coefficients and CD spectra for (a) forward and (b) backward directions.

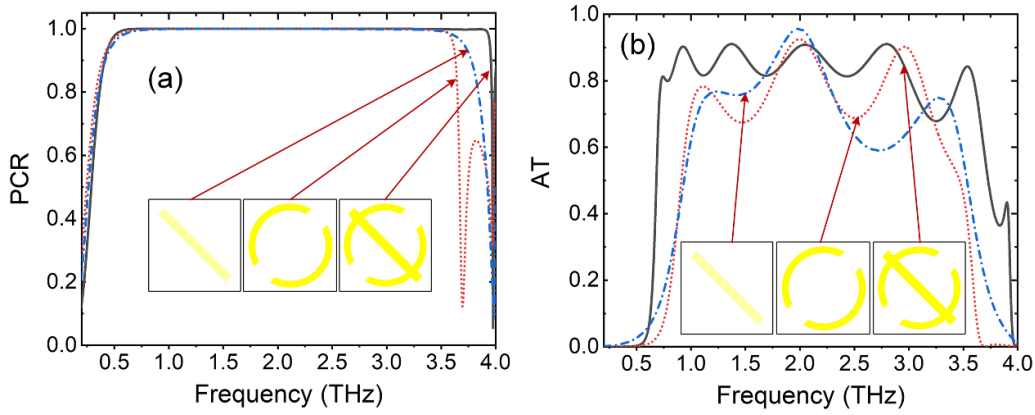


Figure 4. (a) PCR and (b) AT spectra with different shapes of resonance metasurface for forward y-polarized wave.

effect, we simulate the PCR and AT parameters for only strip, only double-split ring, and combination of double-split ring and strip resonators, as shown in figures 4(a) and (b), respectively. At higher frequencies, the PCR efficiency of the strip resonator is higher than that of the double-split resonator. The combination of the double-split resonator and strip resonators significantly enhances the PCR compared to those, as shown in figure 4(a). Furthermore, with the integration of the double-split resonator and strip resonators, the proposed metasurface can improve the AT efficiency across the entire working band of 0.73–3.01 THz, as depicted in figure 4(b). Therefore, it is clear that the combination of the strip with the double-split ring promotes the bandwidth of LPC at higher frequencies and improves the efficiency of the AT parameter over a wide bandwidth.

In practical applications, the incident EM waves are not always perpendicular to the surface of the structure. Hence, it is crucial to investigate the incident angle stability of the metasurface structure. Figure 5 demonstrates the influence of the incident angle on the transmission and PCR performances. As the incidence angle increases up to 80°, the amplitudes of the cross-transmission coefficients (t_{yx} and t_{xy}) decrease across

the investigated frequency range for both the backward x-polarized wave (figure 5(a)) and the forward y-polarized wave (figure 5(b)). This reduction can be attributed to increased absorption losses resulting from the longer effective path length of the wave as the angle of incidence rises. Conversely, the amplitudes of the co-polarized transmission coefficients (t_{xx} and t_{yy}) remain nearly constant at zero across the investigated frequency range for both the backward x-polarized wave (figure 5(a)) and the forward y-polarized wave (figure 5(b)) as the incident angle increases up to 80°. Consequently, although the magnitudes of the cross-polarization coefficients significantly decrease as the incident angle increases up to 80°, they remain substantially larger than those of the co-polarization coefficients. This disparity results in the calculated PCR_x and PCR_y , as described by equations (2) and (3), maintaining an almost constant PCR efficiency above 0.99 across the wide frequency range of 0.57–3.6 THz under both forward y- and backward x-polarized incidences as the incident angle increases up to 80°, as illustrated in figures 5(c) and (d), respectively. This behavior indicates excellent angular insensitivity of the designed structure for LPC.

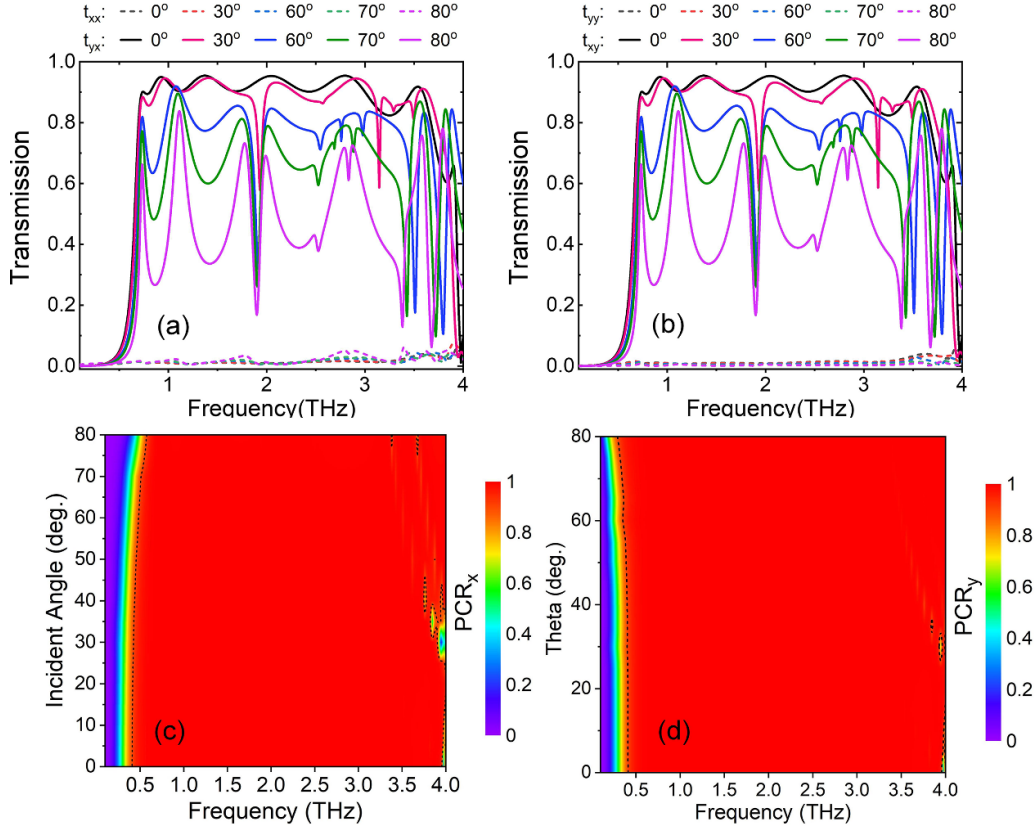


Figure 5. Selected transmission spectra and PCR map as a function of incident angle for (a, c) backward x -polarized wave and (b, d) forward y -polarized wave, respectively. In figure plots the black dashed contour curve indicates the 0.9 PCR efficiency.

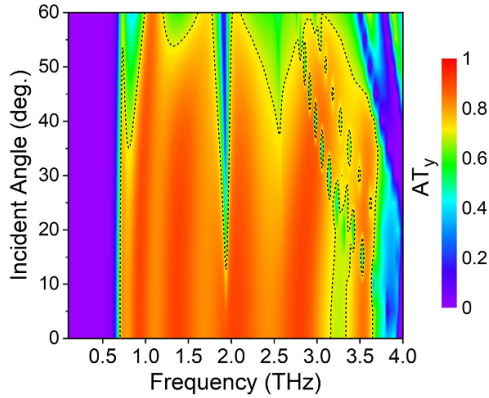


Figure 6. AT efficiency as a function of incident angle for forward y -polarized wave (AT_y). In figure plots the black dashed contour curve indicates the 0.7 AT efficiency.

Figure 6 presents the influence of the incident angle on the AT performance. The AT performance is significantly influenced by the incident angle. The decline in AT performance at oblique incidence can be attributed to destructive effects caused by additional propagation phases as EM waves travel through the dielectric substrate in both directions [28]. However, with an incident angle up to 35° , the AT efficiency can remain as high as 0.7 across the entire operating band, except for a frequency peak near 1.9 THz. The AT efficiency

drops around 1.9 THz, likely due to the strong absorption produced by the resonator shape of the metasurface unit at this frequency [29, 30].

3.2. Mechanisms of transmission polarization conversion

To illustrate the working principle responsible for the transmission polarization conversion characteristics, theoretical analysis is carried out as shown in figures 7(a) and (b). Assuming that the incident EM wave (E_i) is along to the y/x -axis propagating along the forward ($+z$)/backward ($-z$) direction, respectively, decomposed into two orthogonal u - and v -components. The u - and v -axes are rotated $\pm 45^\circ$ to y/x -axis, respectively, as shown in figures 7(a) and (b). For the incident forward y - polarized wave, the incident and transmitted waves can be given as equations (8) and (9), respectively [20, 31].

$$E_i = \hat{y}E_i = \hat{u}E_i + \hat{v}E_i \quad (8)$$

$$E_t = \hat{x}t_{xy}E_i = \hat{u}t_{uu}E_{iu}e^{i\Phi_{uu}} + \hat{v}t_{vv}E_{iv}e^{i\Phi_{vv}} \quad (9)$$

where, \hat{x} , \hat{y} , \hat{u} , \hat{v} are the unit vector, t_{uu} , t_{vv} and Φ_{uu} , Φ_{vv} are the magnitude and phase of u - and v -components of the co-polarization transmission coefficients, respectively. If $t_{uu} = t_{vv}$ and $\Delta\varphi = |\Phi_{uu} - \Phi_{vv}| = 180^\circ + 2k\pi$ (where k is an integer), the synthetic fields of E_{iu} and E_{iv} will align with the x - axis

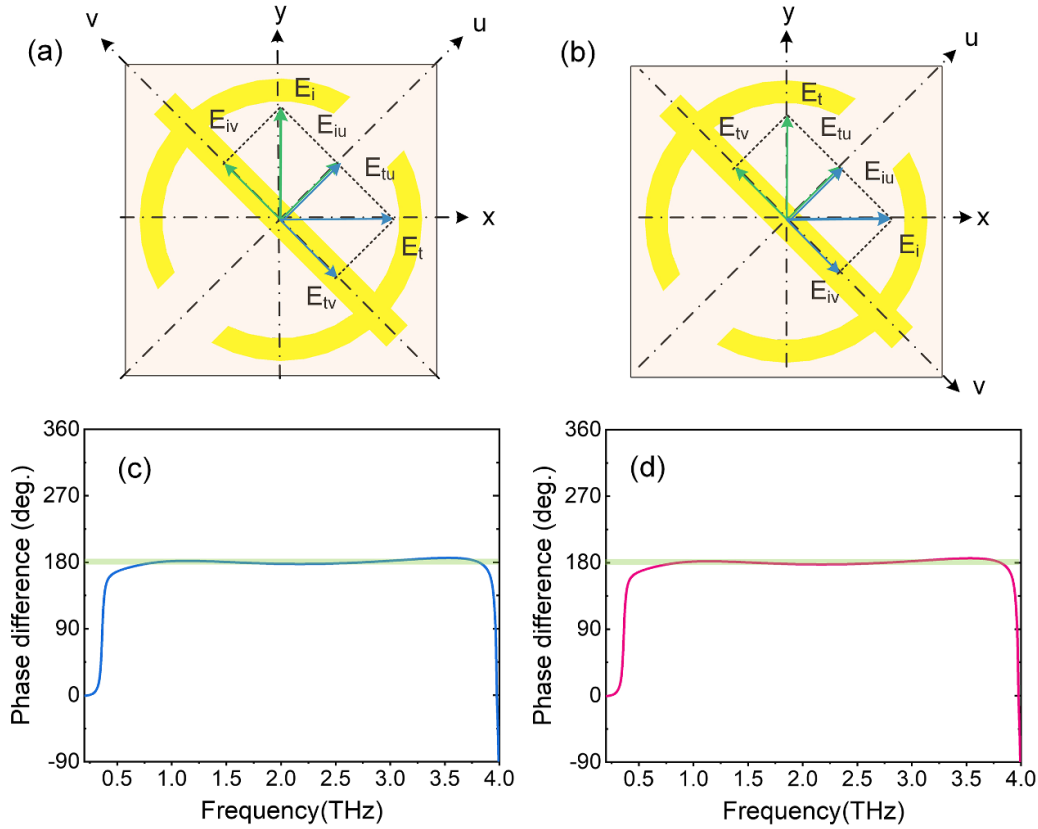


Figure 7. Working principle of the proposed BFM for (a) normal incidence forward y -polarized wave and (b) normal incidence backward x -polarized wave. Phase difference between the decomposed u - and v -components for (c) forward y -polarized wave and (d) backward x -polarized wave.

and y - axis for forward y -polarized waves and backward x -polarized waves, as illustrated in figures 7(a) and (b), respectively. This indicates that the incoming forward y -polarized wave is rotated by 90° , resulting in the action of a transmission cross-polarization converter. Figures 7(c) and (d) show the phase difference of co-polarization in the u - and v -axes directions for incident forward y -polarized wave and backward x -polarized wave, respectively. In figures 7(a) and (b), the phase difference ($\Delta\varphi$) remains near 180° over a broad frequency range of 0.56–3.94 THz. This observation suggests that perfect transmission cross-polarization conversion is achieved within this frequency band.

To explore the transmission polarization conversion mechanism of the proposed BFM, the surface current distributions of the five resonant modes at 0.72, 0.92, 1.37, 2.03, and 2.76 THz are simulated under normally incident on the metasurface. It was reported that the orthogonal metallic gratings act as selectors for x - and y -polarization [21]. When an x -polarized (or y -polarized) incident wave is directed in the forward (or backward) direction, it undergoes reflection, respectively. In this case, the surface current distributions on the orthogonal metallic gratings are nearly negligible as confirmed by simulations (data not shown here). Conversely, a y -polarized (or x -polarized) incident wave can traverse through the upper layer and interact with the middle layer, converting to its

cross polarization. Therefore, to study the physical mechanism behind polarization conversion in the proposed structure that simultaneously realizes the AT effect, which arises from magnetic and/or electric resonances, we examine the surface current distributions of the orthogonal metallic gratings on the top and bottom layers, as well as the middle resonator structure, at the resonant frequencies for a forward y -polarized wave, as shown in figure 8. As seen in figure 8, the surface current distributions on the orthogonal metal gratings is perpendicular, indicating the cross-polarization conversion characteristics of the proposed BFM structure. In figures 8(b) and (h), the surface currents of the resonator structure are concentrated on both the split ring and strip resonators, creating two opposite current loops at the resonant frequencies of 0.72 THz and 1.37 THz. This indicates that magnetic resonance is generated in the upper left and lower right parts of the split rings at these frequencies. In figure 8(e), the surface currents are mainly concentrated on the split ring resonator and are antiparallel to the orthogonal gratings at 0.92 THz, inducing magnetic resonance excited by the incident EM field. Additionally, the parallel direction of the surface currents in the left and right parts of the strip suggests the presence of electric resonance. In figure 8(k), the surface currents are predominantly concentrated on the split ring resonator, with directions parallel to the top gratings layer and antiparallel to the bottom gratings layer

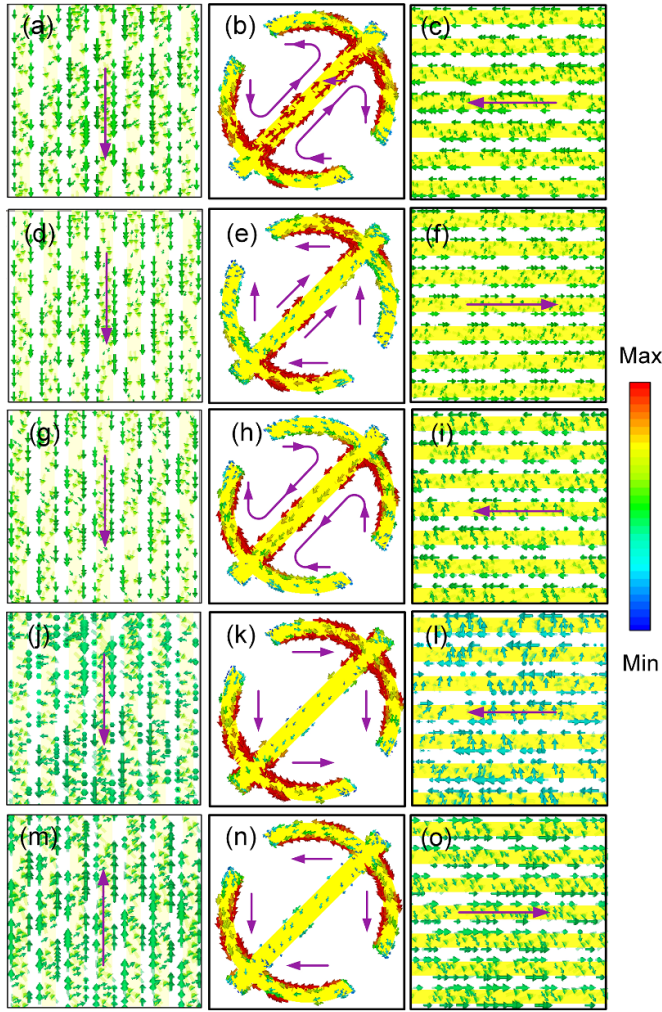


Figure 8. Surface current distributions on the top grating, resonance structure, and bottom grating layers for forward y -polarized wave at various resonant frequencies of (a–c) 0.72 THz, (d–f) 0.92 THz, (g–i) 1.37 THz, (j–l) 2.03 THz, and (m–o) 2.76 THz, respectively.

at 2.03 THz, inducing both electric and magnetic resonances. In figure 8(n), the surface currents are mainly concentrated on the split ring resonator, with current directions opposite to those of the orthogonal metal grating at 2.76 THz, generating magnetic resonance between the resonator structure and the orthogonal metal gratings. These observations indicate that the superposition of magnetic and electric resonances contributes to the bandwidth expansion of transmission polarization conversion.

3.3. Influence of structural parameters

To understand the influence of the geometrical parameters of the proposed structure on the PCR and AT characteristics, numerical simulations are performed with changing one variable and fixing other parameters for forward y -polarized waves. Figure 9 shows the influence of structural parameters P and d on PCR and AT efficiencies when other parameters

are fixed. As seen in figures 9(a) and (b), as the thickness (d) increases from $13\ \mu\text{m}$ to $21\ \mu\text{m}$ in steps of $0.5\ \mu\text{m}$, the PCR bandwidth slightly narrows, while the AT bandwidth fluctuates significantly. The AT bandwidth, defined by AT efficiency above 0.8, widens with increasing d up to $17\ \mu\text{m}$. However, with d value higher than $1.7\ \mu\text{m}$, the AT bandwidth deteriorates. Thus, considering both PCR and AT bandwidths, $d = 17\ \mu\text{m}$ is the optimal value. A similar trend is observed when the period (P) increases from $38.5\ \mu\text{m}$ to $45.5\ \mu\text{m}$ in steps of $0.7\ \mu\text{m}$ (figures 9(c) and (d)). This indicates that $P = 42\ \mu\text{m}$ is the optimal value.

The influence of structural parameters i and l on PCR and AT efficiencies is illustrated in figures 10(a), (c) and (b), (d), respectively. The PCR efficiency and bandwidth of the proposed BFM are hardly affected by the structural parameters i and l . Meanwhile, the AT bandwidth undergoes significant changes with varying the values of i and l . The AT bandwidth is widest with the optimized values of $i = 4\ \mu\text{m}$ and l in the range of $42.5\text{--}45.5\ \mu\text{m}$.

Furthermore, the influence of other geometrical parameters R , b , and c on PCR and AT efficiencies is also investigated and depicted in figures 11. The PCR bandwidth of the proposed BFM shows insensitivity to the structural parameters of R , b , and c , as illustrated in figures 11(a), (c), and (e), respectively. In contrast, AT exhibits significant variation with changes in R , b , and c . The widest AT bandwidth is observed at $R = 18.7\ \mu\text{m}$, $b = 3.0\ \mu\text{m}$, $c = 10\ \mu\text{m}$, which are chosen as the optimal values for these structural parameters. The above analysis results indicate that while PCR remains hardly affected by geometric parameters, the bandwidth of AT can be notably influenced.

Besides the dimensional parameters of the structure, the influence of the dielectric material properties on the performance of the proposed BFM structure is investigated. The PCR and AT spectra are simulated by varying the loss tangent and dielectric constant of the dielectric material within the ranges of 0.007 to 0.057 and 2.0 to 5.0, respectively, as shown in figures 12(a)–(d). As illustrated in figure 12(a), both the PCR bandwidth and efficiency remain unchanged with variations in the loss tangent within this range. However, the AT efficiency shows a slight decrease with increasing loss tangent while remaining above 0.8 when the loss tangent is below 0.027, as shown in figure 12(b). As the dielectric constant increases from 2.0 to 5.0, both the PCR and AT spectra shift to higher frequencies (figures 12(c) and (d)). Additionally, the PCR efficiency remains above 0.99 (figure 12(c)), while the AT efficiency decreases but stays above 0.8 when the dielectric constant is below 3.5 (figure 12(d)). These findings demonstrate that the PCR and AT performance of the proposed BFM structure remains highly efficient across a wide range of dielectric properties, particularly with a loss tangent below 0.027 and a dielectric constant below 3.5. This suggests that the BFM structure can be fabricated using a variety of commercially available dielectric materials.

By analyzing and discussing the results from the three aforementioned sections, it can be seen that the proposed

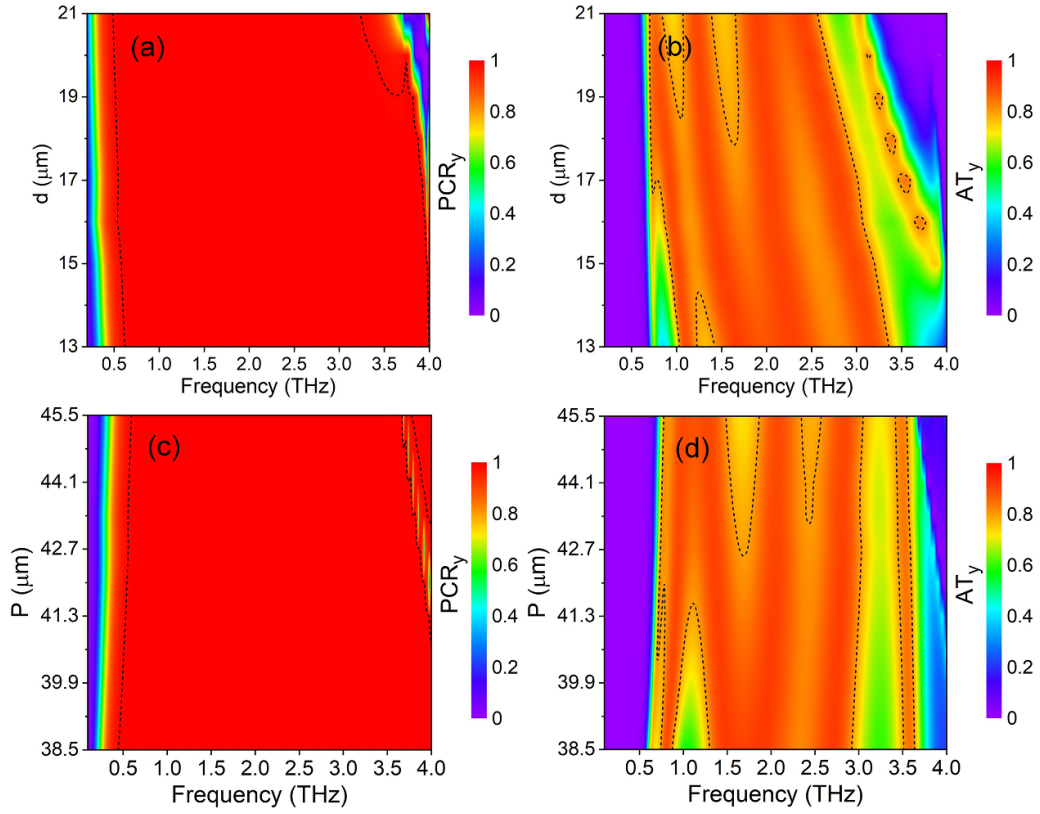


Figure 9. PCR and AT efficiencies as a function of (a), (b) d and (c), (d) P values for forward y -polarized wave, respectively. In figure plots the black dashed contour curve indicates the 0.99 and 0.8 PCR and AT efficiencies, respectively.

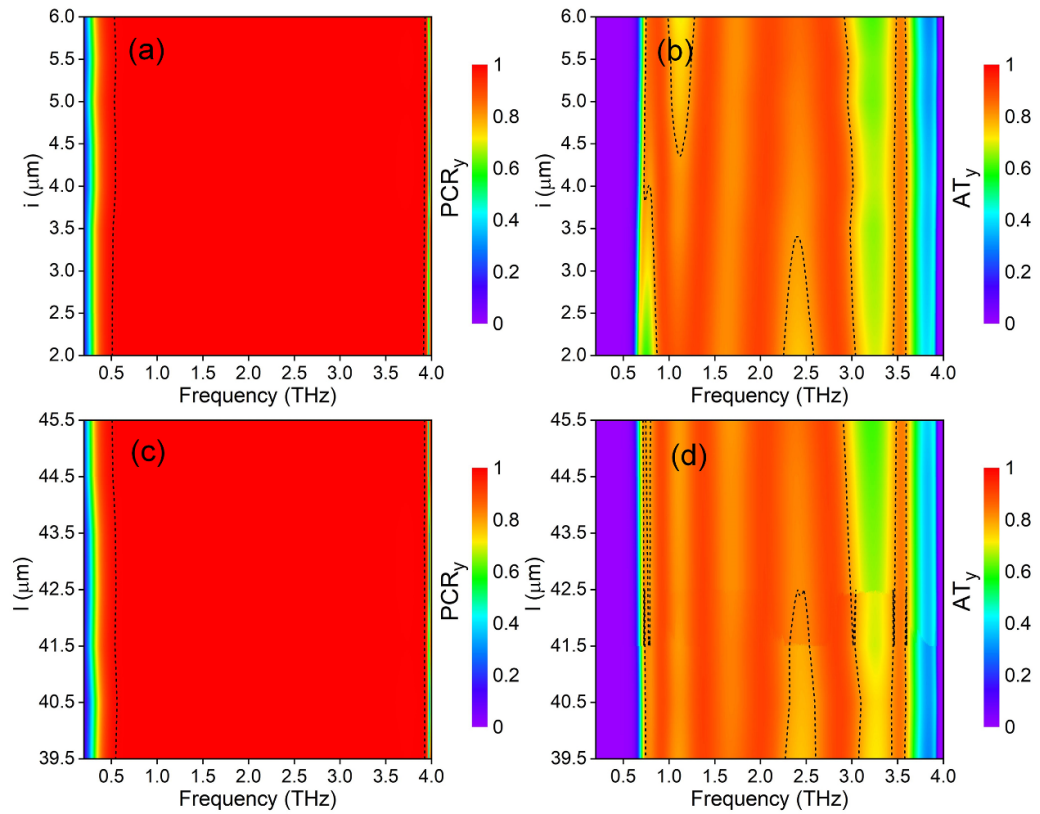


Figure 10. PCR and AT efficiencies as a function of (a), (b) i and (c), (d) l values for forward y -polarized wave, respectively. In figure plots the black dashed contour curve indicates the 0.99 and 0.8 PCR and AT efficiencies, respectively.

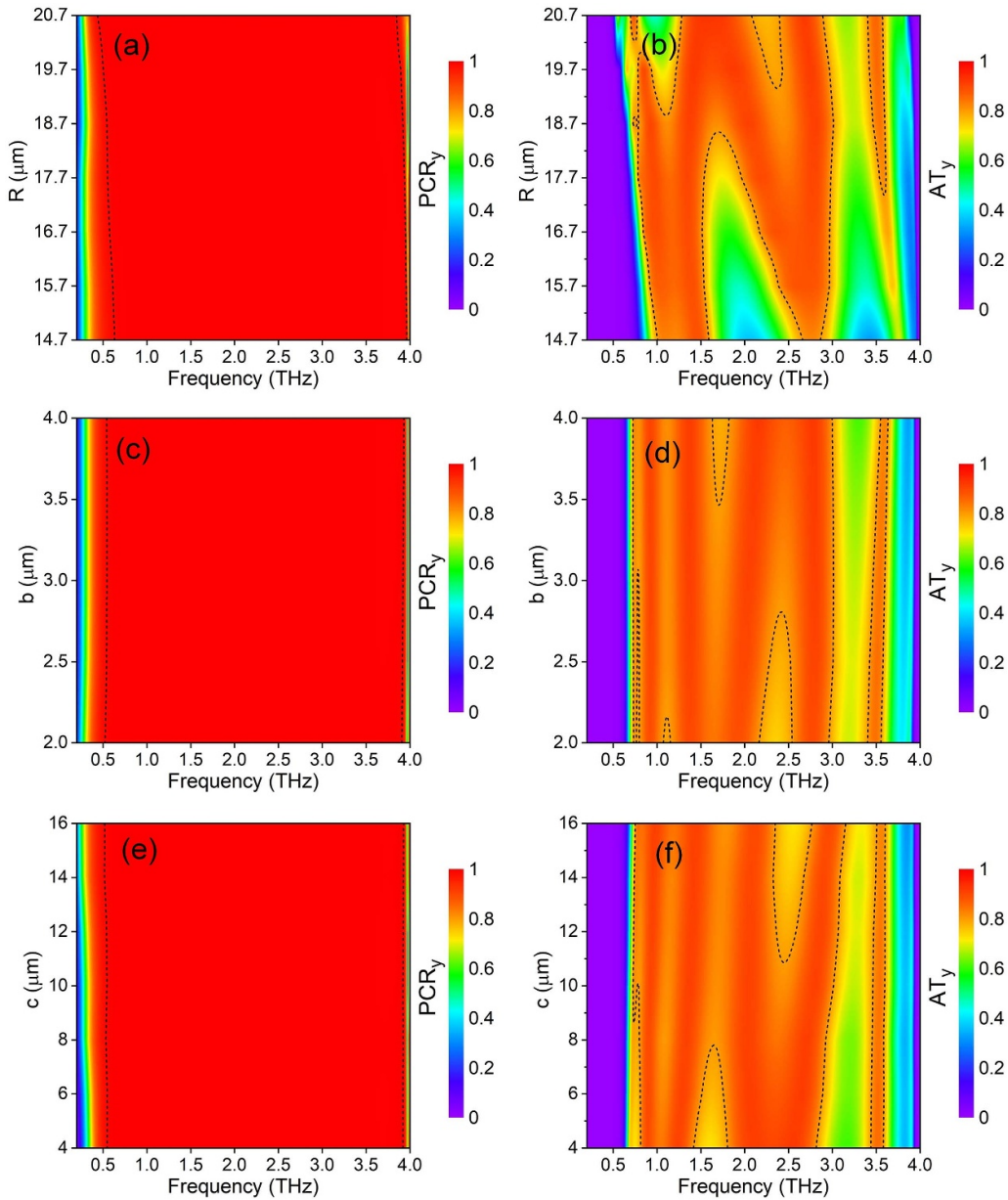


Figure 11. PCR and AT efficiencies with different parameters of (a), (b) R , (c), (d) b , and (e), (f) c values for forward y -polarized wave, respectively. In figure plots the black dashed contour curve indicates the 0.99 and 0.8 PCR and AT efficiencies, respectively.

structure exhibits perfect PCR and a high AT effect across a wide bandwidth in the THz region. To emphasize the advantages of the proposed BFM structure, we have compared it with previous works exhibiting similar characteristics, as illustrated in table 1. The comparison includes the working band for LPC and AT functionalities, along with their corresponding

RBW and efficiency. Our design, when compared with similar metasurfaces in the THz range, achieves superior wide-band performance and high efficiency in both PCR and AT, suggesting significant potential for the proposed structure in a wide range of THz applications, including imaging, sensing, and communication.

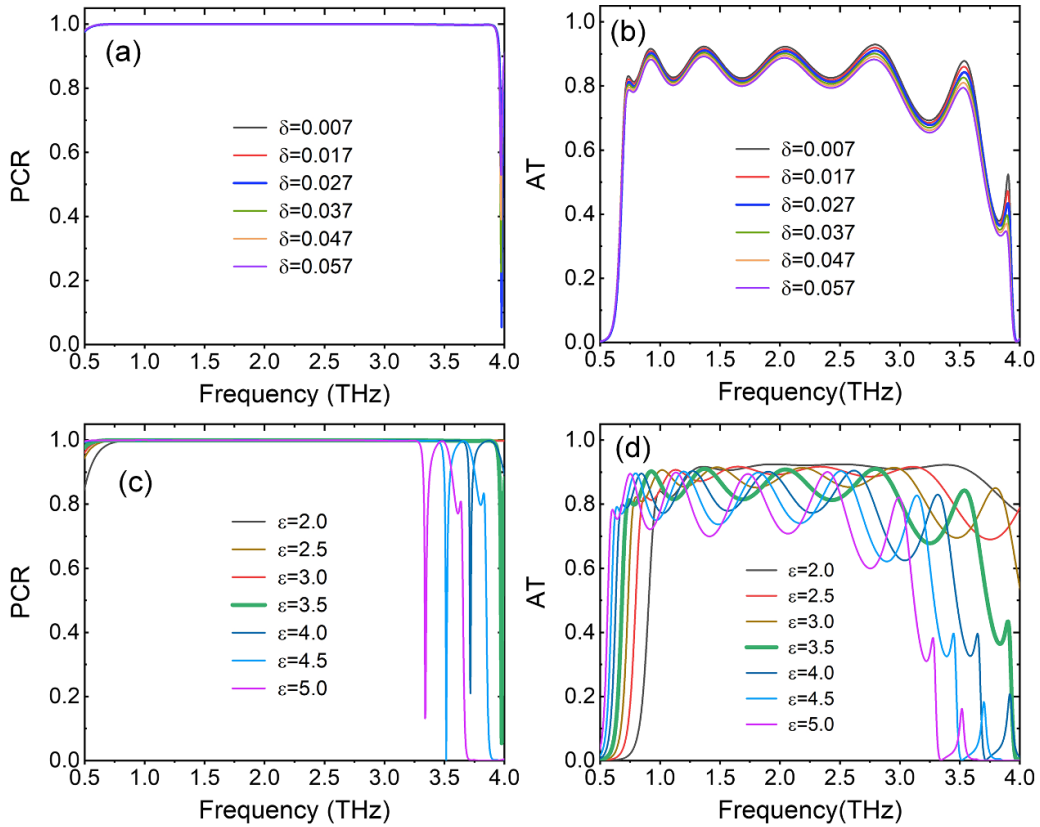


Figure 12. The dependence of PCR and AT efficiencies as a function of (a), (b) the loss tangent and (c), (d) dielectric constant of the dielectric layer of the proposed BFM structure, respectively.

Table 1. Performance comparison of the proposed BFM with previous works in the THz range.

References	Function	Working Band (THz)	RBW (%)	Efficiency
[32]	LPC	0.2–1.6	155.6	0.99
	AT	~0.54–1.38	87.5	0.6
[25]	LPC	1.67–2.05	20.4	0.9
	AT	1.67–2.05	20.4	0.6
[20]	LPC	0.41–2.38	141.22	0.99
	AT	0.5–2.41	131.27	0.64
[33]	LPC	NA	NA	NA
	AT	124–244	65.22	0.8
Our work	LPC	0.56–3.94	150.2	0.99
	AT	0.73–3.01	124.9	0.8

4. Conclusion

A wideband and high efficient BFM based on a three-layer structure comprising orthogonal metal gratings, a metal resonator, and a polyimide dielectric spacer was proposed. By integrating double-split ring and strip resonator, our design achieves effective LPC and AT capabilities. The underlying physical mechanism driving wideband transmission polarization conversion was comprehensively elucidated using theoretical analysis and surface current distribution analysis. The proposed BFM reveals effective LPC across a broad frequency

range of 0.56–3.94 THz with PCR exceeding 0.99 and AT effect from 0.73–3.01 THz with performance surpassing 0.8. The wideband and high-efficiency of both LPC and AT were maintained for wide incident angles. This design shows significant promise for applications in imaging, sensing, and communication.

Data availability statement

All data that support the findings of this study are included within the article (and any supplementary files).

Author contributions

TQHN contributed to the conception of the paper. TQH Nguyen, TM Nguyen, and HQ Nguyen performed simulations and analyzed the data. TQH Nguyen wrote the paper. All the authors revised the paper.

Conflict of interest

The authors declare no competing interests.

ORCID iD

Thi Quynh Hoa Nguyen  <https://orcid.org/0000-0002-0955-8241>

References

- [1] Das S, Anveshkumar N, Dutta J and Biswas A 2021 *Advances in Terahertz Technology and Its Applications* (Springer)
- [2] Pawar A Y, Sonawane D D, Erande K B and Derle D V 2013 *Drug Invention Today* **5** 157–63
- [3] Wallace V P, MacPherson E, Zeitler J A and Reid C 2008 *J. Opt. Soc. Am. A* **25** 3120–33
- [4] Landy N I, Sajuyigbe S, Mock J J, Smith D R and Padilla W J 2008 *Phys. Rev. Lett.* **100** 207402
- [5] Nguyen T Q M, Nguyen T K T, Le D T, Truong C L, Vu D L and Nguyen T Q H 2021 *Plasmonics* **16** 1583–92
- [6] Phan D T, Nguyen T K T, Nguyen N H, Le D T, Bui X K, Vu D L, Truong C L and Nguyen T Q H 2021 *Phys. Status Solidi b* **258** 2100175
- [7] Wang Y, Guan C, Ding X, Zhang K, Ratni B, Burokur S N, Gu X and Wu Q 2019 *Opt. Lett.* **44** 2189–92
- [8] Fan Y, Yao J and Tsai D P 2023 *Light: Sci. Appl.* **12** 15
- [9] Cao T N, Nguyen M T, Nguyen N H, Truong C L and Nguyen T Q H 2021 *Mater. Res. Express* **8** 065801
- [10] Rahman Qureshi U U and Basir S 2024 *Opt. Mater.* **149** 115044
- [11] Qureshi U U R, Khan M I and Hu B 2023 *Phys. Scr.* **98** 075513
- [12] Fedotov V A, Mladyonov P L, Prosvirnin S L, Rogacheva A V, Chen Y and Zheludev N I 2006 *Phys. Rev. Lett.* **97** 167401
- [13] Wang Y H, Kim I, Jin R C, Jeong H, Li J Q, Dong Z G and Rho J 2018 *RSC Adv.* **8** 38556–61
- [14] Khan M I, Hu B, Chen Y, Ullah N, Khan M J I and Khalid A R 2020 *IEEE Antennas Wirel. Propag. Lett.* **19** 1137–41
- [15] Li J S and Bai F Q 2020 *Opt. Mater. Express* **10** 1853–61
- [16] Tian Y, Chen Z, Ren F F, Du Q and Li Z 2021 *Front. Phys.* **9** 676840
- [17] Bibi A, Khan M I, Hu B, Iqbal S and Khan I 2022 *Int. J. RF Microw. Comput. Aided Eng.* **32** e23224
- [18] Zhao J, Li N and Cheng Y 2023 *Chin. Opt. Lett.* **21** 113602
- [19] Huang X, Ma X, Gao H, Guo L and Li X 2023 *Appl. Phys. A* **129** 278
- [20] Zhang Y, Luan W, Yan X, Gao X, Zeng X, Jin Z, Ma G and Yao J 2022 *Appl. Phys. B* **128** 156
- [21] Qureshi U U R, Deng B, Wu X, Xiong C, Jalal A, Khan M I and Hu B 2024 *Opt. Express* **32** 32836–48
- [22] Nguyen T M, Vu D L, Nguyen T Q H and Kim J M 2022 *Sci. Rep.* **12** 18779
- [23] Phan H L, Nguyen T Q H and Kim J M 2024 *IEEE Access* **12** 11664–73
- [24] Menzel C, Rockstuhl C and Lederer F 2010 *Phys. Rev. A* **82** 053811
- [25] Lv F, Wang L, Xiao Z, Chen M, Cui Z and Xu Q 2021 *Opt. Mater.* **114** 110667
- [26] Wei Z, Zhao Y, Zhang Y, Cai W, Fan Y, Wang Z and Cheng X 2022 *Nanoscale Adv.* **4** 4344–50
- [27] Li J et al 2021 *Opt. Express* **29** 28329–37
- [28] Liu C, Gao R, Wang Q and Liu S 2020 *J. Appl. Phys.* **127** 153103
- [29] Diem M, Koschny T and Soukoulis C M 2009 *Phys. Rev. B* **79** 033101
- [30] Wu Y, Huang S, Deng L, Tang C, Gao X, Fang S and Qiu L L 2022 *Results Phys.* **40** 105859
- [31] Fu C, Dong S, Liu L, Zhang L, Yu W, Wang X, Liu X and Han L 2023 *Opt. Commun.* **546** 129733
- [32] Zhao J, Song J, Xu T, Yang T and Zhou J 2019 *Opt. Express* **27** 9773–81
- [33] Wang C, Zhou X, Tang D, Pan W and Dong J 2018 *Optik* **164** 171–7